Diamond & Related Materials 146 (2024) 111237

Contents lists available at ScienceDirect

Diamond & Related Materials

journal homepage: www.elsevier.com/locate/diamond

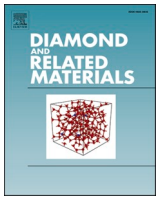

Making the diamond vortex phase masks for the METIS instrument

Pontus Forsberg [a,*], Petri Karvinen [b], Samuel Ronayette [c], Markku Kuittinen [b], Olivier Absil [d], Lorenzo König [d], Christian Delacroix [d], Gilles Orban de Xivry [d], Jean-Christophe Barrière [e], Eric Pantin [c], Mikael Karlsson [a,*]

[a] Department of Materials Science and Engineering, Uppsala University, Sweden
[b] Center for Photonics Sciences, University of Eastern Finland, Finland
[c] Université Paris-Saclay, Université Paris Cité, CEA, CNRS, AIM, Gif-sur-Yvette, France
[d] STAR Institute, University of Liège, Belgium
[e] Université Paris-Saclay, CEA, DRF/IRFU/DIS, Gif-sur-Yvette, France

ARTICLE INFO

Keywords:
Diamond microfabrication
Reactive ion etching
Optical gratings
Infrared optics
Astronomy
Exoplanets

ABSTRACT

Direct observation of exoplanets and proto-planetary disks with the METIS instrument at the Extremely Large Telescope will provide new insights into the processes of planet formation and exoplanet atmospheres. This will be possible thanks to a powerful vector vortex coronagraph that can suppress the starlight to reveal faint signals around it. Here we present the process of making the phase masks at the heart of the coronagraph. These annular groove phase masks consist of deep sub-wavelength gratings in diamond that are etched using inductively coupled oxygen plasma with a strong bias. The METIS instrument requires a wider bandwidth than such components have previously been demonstrated for, leading to a grating design with higher aspect ratio and more vertical walls. To achieve this, the etch mask used for diamond etching was changed from aluminium to silicon and the plasma power was increased. We also improved on our method for reducing the grating depth of finished components to fine-tune them. Together with improved optical testing, this allowed us to produce the best vortex phase masks so far demonstrated for the astronomical N-band.

1. Introduction

METIS, the "Mid-infrared ELT Imager and Spectrograph", will be one of the first generation of instruments at the European Southern Observatory's Extremely Large Telescope (ELT). Working in the L, M and N bands between 3 and 13 μm wavelength (the astronomical bands are wavelength bands where the Earth's atmosphere is transparent), METIS will be a multipurpose instrument. In particular, it is expected to make large contributions to our knowledge of exoplanets and planet formation through direct observations [1]. Observations of faint planets and proto-planetary disks close to bright stars are made possible by the implementation of a powerful vector vortex coronagraph, an instrument that blocks out the starlight while letting the light from nearby objects through. At the heart of the METIS coronagraphs sit phase masks which cancel out the starlight through destructive interference to make nearby exoplanets visible. These phase masks are so-called Annular Groove Phase Masks (AGPMs) [2]. An AGPM is a circular sub-wavelength grating (Fig. 1) that through form birefringence gives rise to a so-called vector vortex phase mask [3], i.e. a half wave plate with an optical axis that turns smoothly around the center of the mask. Starlight focused on the center of the phase mask will be redirected outwards of the telescope pupil and can be blocked by a Lyot-stop aperture in a downstream pupil plane. Light from an exoplanet, on the other hand, passes through the mask away from the center without being redirected.

We use diamond for the AGPMs because of its transparency at infrared wavelengths. Especially at long wavelengths (around 10 μm and above), the list of useable materials becomes fairly short and exotic. Some potential materials, such as germanium, have very high refractive indices, for which we have not found a good solution for a wideband AGPM. Other materials, such as zinc selenide, are difficult to etch with sufficient precision. Diamond has a suitable refractive index of 2.38 [4] and though diamond is extremely hard, it can be dry etched using oxygen plasma [5–17]. Besides the refractive index, the hardness, chemical resistance and low thermal expansion of diamond are also advantageous as they make the component more robust. The oxygen plasma used to etch diamond puts high demands on the etch mask. Common choices of

* Corresponding authors.
E-mail addresses: pontus.forsberg@angstrom.uu.se (P. Forsberg), mikael.karlsson@angstrom.uu.se (M. Karlsson).

https://doi.org/10.1016/j.diamond.2024.111237
Received 22 March 2024; Received in revised form 16 May 2024; Accepted 23 May 2024
Available online 24 May 2024

mask material in the literature include aluminium, gold, silicon oxide and silicon nitride [5,13,14]. Typically, the selectivity (i.e. the etch rate in diamond divided by that in the mask material) and micromasking due to redeposited mask material are the most important characteristics of the mask [14]. To etch high aspect ratio gratings in diamond, a thick mask (similar thickness as the width of the grooves) with vertical edges helps keep redeposited material from the bottom of the grating [5]. We have described this in our previous work where we used thick aluminium (Al) masks [5,7] and high aspect ratio diamond gratings have also been made for X-ray beam splitting using thick hydrogen silsesquioxane [16] and gold [17] masks.

In the last decade we have made AGPMs for instruments at several large telescopes, such as the European Very Large Telescope, the Large Binocular Telescope and the Keck Telescope [5–8,18]. Most of these have been for the astronomical L-band, but we have also made AGPMs for the K- M- and N-bands (these bands are atmospheric transmission windows in the near and mid infrared). The latest AGPMs produced for the N-band were for the NEAR experiment, a part of Breakthrough Watch [19]. These were installed in the VISIR instrument of the Very Large Telescope and used to search for earth-like planets around α Centauri. New for the METIS AGPMs is the wider spectral bandwidth, going up to 50 % bandwidth, while the previous components were typically designed to cover a 20 % bandwidth [6]. To produce these gratings with high precision we have improved several critical steps compared to our previous process: patterning, masking, etching, optical evaluation, and tuning the grating.

the L-, M- and N-bands. These components were designed for wider bandwidths than previously manufactured AGPMs; the L-band AGPM will cover wavelengths between 2.9 and 4.1 μm, the M-band AGPM between 3.9 and 5.3 μm, and the N-band AGPM between 8.1 and 13.1 μm. The performance was simulated using Rigorous Coupled Wave Analysis (RCWA) [20] of a one-dimensional grating in MATLAB, with code based on Pavel Kwiecien's RCWA-1D.[1] For the calculations, the grating cross section was approximated as trapezoidal, which in the RCWA is implemented as a layered structure with a small change in width in each layer. The parameters defining the grating are line width, depth, wall angle and period (Fig. 1). The performance metric of the phase mask is null depth, which is a measure of how well the light focused on the centre of the AGPM is cancelled, compared to light from the same source focused some distance from the centre. The null depth can be calculated from the transmission and phase delay of the polarizations calculated with RCWA [21]. An example of a calculated null depth map can be seen in Fig. 2. The null depth specifications for METIS (Table 1) are set to ensure that the leakage of stellar light due to the phase mask is negligible compared to other sources. To maintain the sub-wavelength criterion, the period of the grating scales with the shortest wavelength in the band. The line width scales similarly to maintain roughly the same fill factor. The depth of the grating instead scales roughly with the centre wavelength of the band. Taken together this means that an AGPM designed for a wider band will typically require a higher aspect ratio of the grating grooves (defined as (P-w)/h with the notation in Fig. 1). A wider band also makes it more difficult to

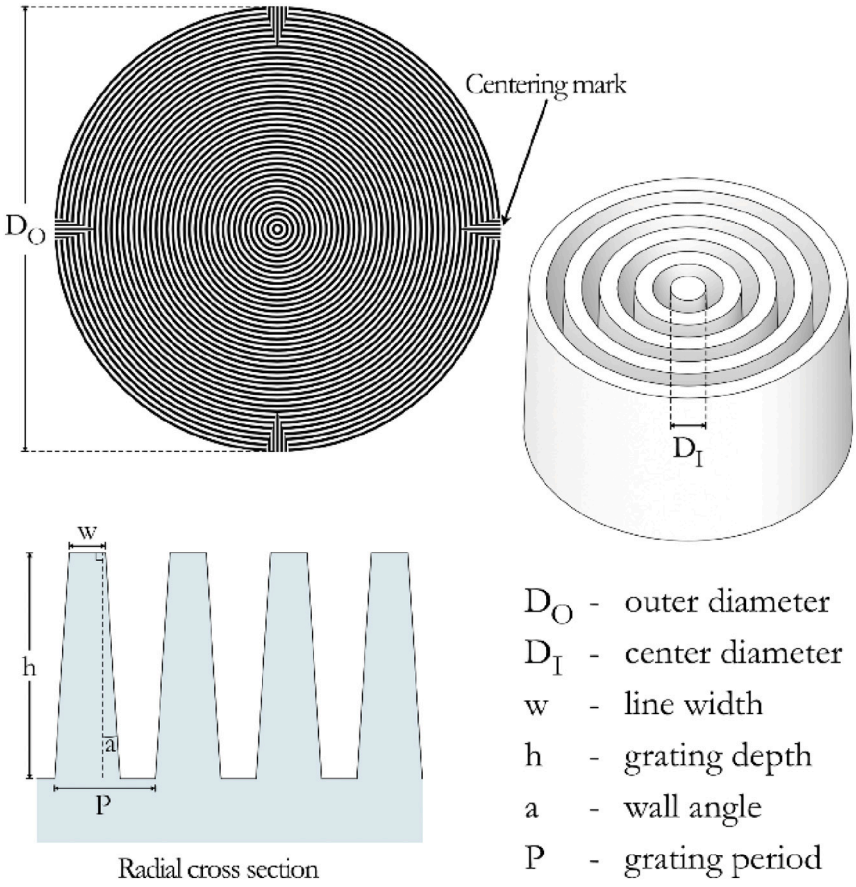

Fig. 1. Schematic view of the AGPM. Note that for visibility the number of rings has been reduced to a few tens in the drawing while the actual components have thousands.

1.1. AGPM design

The METIS instrument will have AGPMs for three wavelength bands,

[1] https://sourceforge.net/projects/rcwa-1d/

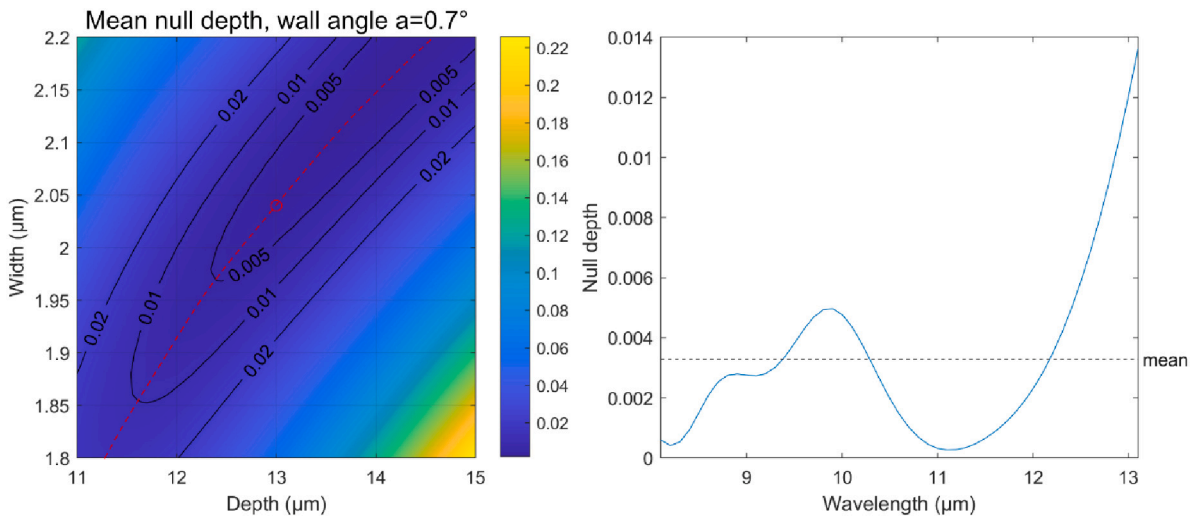

Fig. 2. Null depth calculations. Left: A map of mean null depth between 8.1 and 13.1 µm wavelength. The wall angle is fixed at 0.7°. The dashed red line illustrates the optimal depth for a given width. Right: Null depth as a function of wavelength at the point marked with a red circle on the map. (For interpretation of the references to colour in this figure legend, the reader is referred to the web version of this article.)

Table 1
Wavelength bands and their grating periods and performance specifications.

Band	Wavelengths	Grating period	mean null depth	Max null depth
L	2.9–4.1 µm	1.2 µm	< 1/500	< 1/100
M	3.9–5.3 µm	1.6 µm	< 1/500	< 1/100
N	8.1–13.1 µm	3.4 µm	< 1/100	< 1/20

find grating parameters that give good enough performance over the whole band. This means that higher precision is required in the fabrication. Previous N-band AGPMs have typically had wall angles between 2.9° and 3.4°. While it is possible to find a solution with an angle at the lower end of this range that meets the METIS specification, it is close to where the walls of the grating meet in a sharp V-shape at the bottom. When the groove becomes very narrow near the bottom, the etch rate becomes more difficult to predict. Once the walls meet, etching nearly stops completely. This means that small variations in line width and wall angle can give rise to larger errors in depth, and a slightly too high angle or too wide line width might make it impossible to reach the right depth. Therefore, we have made changes to our fabrication process to reduce the wall angle. As with previous AGPMs, we can compensate for small errors in line width (or wall angle) by adjusting the depth (Fig. 2).

The diameter of the pillar at the center of the AGPM (D_I in Fig. 1) was set to 1.62 times the line width [22]. The outer diameter of the grating was 15 mm for the N-band and 20 mm for the L- and M-bands. Close to the edge of the component four centering marks were included in the design (Fig. 1), to help with aligning the component in test benches and the instrument. These are wedges, pointing at the centre of the phase mask, with a grating perpendicular to the AGPM grating, which makes them clearly visible both under a microscope and to the naked eye. To reduce reflections, which can cause unwanted stray light and ghost signals in the instrument, an anti-reflective grating was etched on the back side of the diamond substrate [10]. This is a square grating with the same period as the AGPM, but etched to a much shallower depth.

In this paper we will focus on the manufacturing of the N-band components. These were in many ways the most challenging to make, since they cover a wider relative bandwidth and require much deeper grooves in the diamond than the AGPMs for the other bands. The N-band AGPMs for METIS also differ the most from previously published AGPMs in the same wavelength band. For the L- and M-band AGPMs, the fabrication was similar to high bias power diamond etching we have described previously [7], though we switched to a silicon (Si) mask.

2. Methods

Polycrystalline diamond substrates of optical quality, 15 mm in diameter and 300 µm thick, were bought from Diamond Materials GmbH (Freiburg, Germany). All substrates were marked with a number close to the edge on the front (growth) side by laser ablation, to avoid any mix-ups.

The process steps for etching the AGPM in diamond (the same steps are followed for the anti-reflective grating on the back) are shown in Fig. 3. Etching a deep diamond grating in an oxygen plasma required a hard mask. This hard mask was in turn etched using a thin polymer mask. The polymer was patterned by a solvent assisted micromolding (SAMIM) method from a master pattern on a silicon wafer. All processing was carried out in a clean room environment (ISO class 5 to 7) with controlled temperature and humidity.

The AGPM master was patterned using electron beam lithography (Raith EBPG5000 + ESHR). The pattern was exposed (220 µC/cm^2) directly onto the 500 nm thick resist film (AR-P 6200, Allresist GmbH), developed in a puddle developer for 60 s in Ethyl 3-Ethoxypropionate (EEP) and then rinsed using isopropanol. The line width was increased by 100 nm on the master patterns compared to the AGPM design, to compensate for typical shrinkage that we see during the masking process (below).

Previous N-band AGPM patterns have been written by laser, which often led to small line width variations depending on angle, possibly due to astigmatism of the laser. Electron beam lithography (which we have previously used for AGPMs for shorter wavelengths) should give a more consistent line width.

For a small period grating with high aspect ratio, the demands on the mask are quite different than when etching structures with larger lateral dimensions [5]. Mask erosion due to sputtering by high energy ions is typically much higher at the edges of the mask, and in a grating every part of the mask is close to an edge. Since the sputter yield is highly dependent on the angle of incidence, the shape of the edge also plays a large role. Especially at the start of etching, it is important to have near vertical sides on the mask to keep the redeposition low. Further on in the etching, the role that redeposited material plays is different when the tightly spaced walls of the grating leads to most redeposited mask material sticking to a wall rather than the bottom [5]. Previous AGPMs have been etched using Al for the hard etch mask [5–8]. This has resulted in high performing components, but there have been a few downsides to this choice of material. One is that the sputtered Al film is

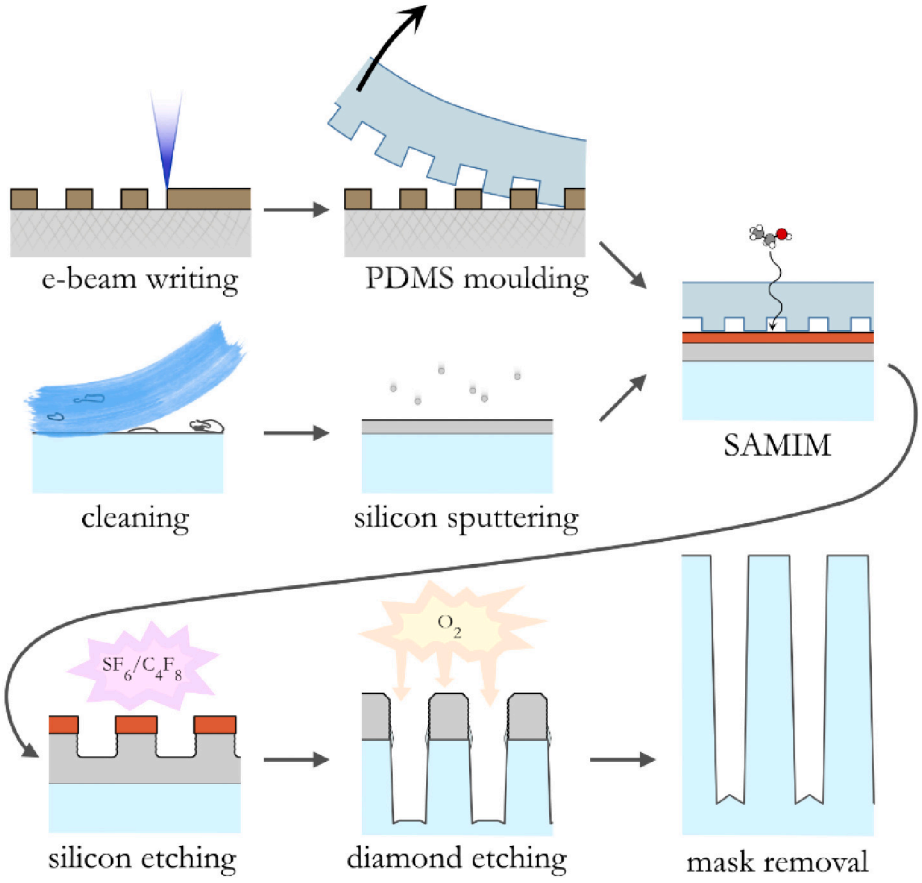

Fig. 3. Schematic view of the processing steps.

typically a bit rough, especially the thick films needed for the N-band. This film roughness translates into a small amount of roughness in the edges of the final grating. Another downside to the Al mask is that in order to etch a thick Al film with vertical walls, we needed additional mask layers between the resist and the Al. These masking layers increase the number of process steps for both deposition and etching and also contribute to more variation in line width between components. Finally, the Al is sputtered from the edges of the mask during etching. This material is deposited and builds up on the opposite side of the etched grooves, which plays a major role in increasing the wall angle of the grating [5,7]. Here we have used Si instead of Al for the diamond etch mask. Depositing the Si film through sputtering was slower than Al, but the deposited film was smoother. Further, the Si mask can be etched with just a few hundred nanometers of photoresist as mask. Preliminary tests have shown that Si is removed faster than Al during diamond etching, leading to lower selectivity, but the re-deposited material is not as tightly focused on the opposite wall, so the diamond can be etched with more vertical walls.

Before being coated with Si the substrates were cleaned by rinsing in acetone, isopropyl alcohol, and water and then put in heated piranha solution (H_2SO_4 and H_2O_2 mixture) for 30 min and then rinsed in water.

Si was sputtered with a Von Ardenne CS730S magnetron sputter system with a pulsed DC power of 500 W. The first 300 s of sputtering was done at an argon pressure of 1.5 μBar, the low pressure was found to improve adhesion. This was followed by eight 270 s rounds of sputtering at 6 μBar pressure, with five minutes in between to allow heat to dissipate. The resulting film was 2.2 μm thick.

The SAMIM process used to copy the e-beam written AGPM pattern to the Si coated diamond substrate consists of several steps. First a mould of the master pattern is made in a permeable silicone elastomer. A thin film of ethanol soluble polymer is then deposited on the substrate. The elastomer mould is placed on top of the polymer film and the stack is placed in ethanol vapor. The vapor permeates through the mould and liquifies the polymer, which fills the mould due to capillary forces. After baking to remove the ethanol, the mould can be removed. This method is suitable for replicating gratings with small period. It tends to fail if the features are too wide (capillary action fails to move the polymer evenly) or the depth or fill factor changes too much across the surface. The thickness of the polymer film should be adjusted to the pattern so that the dissolved polymer can fill the mould with very little left over. Too much will give a thick residual layer and too little will give voids in the features.

The elastomer used for the mould was polydimethylsiloxane (PDMS, Wacker Elastosil RT601). After mixing the two components, a small amount was dripped on the master pattern, spread to around half millimetre thickness with pressurized air, and left to relax for 15 min. After baking for 15 min at 75 °C, the hardened PDMS was peeled from the master pattern. The Si coated diamond substrate was coated with Shipley S1813 photoresist, which is both ethanol soluble and suitable as mask for Si in the dry etching process. The film thickness was controlled by varying the dilution of photoresist with AZ EBR 70/30 solvent (MicroChemicals) before spin coating at 6000 rpm for 30 s. After spin coating, the resist was baked for 60 s at 115 °C to remove the solvent. The PDMS mould was placed on top of the baked resist by hand. This was a delicate step as the AGPM pattern on the mould needs to be aligned with the substrate while avoiding both bending the mould and trapping air under it. The sample was placed in ethanol vapor for 30 min in a covered crystallizing dish. Ethanol was then removed by baking for 5 min at 50 °C and 5 min at 60 °C before the mould was peeled off. After a one-minute hard bake at 115 °C, the sample was ready for etching.

Silicon and diamond dry etching was done in a Tegal 110 S/DE deep reactive ion etch system. Compared to the old PlasmaTherm etcher we

used for previous AGPMs, this system is similar in that it is also an inductively coupled plasma (ICP) etcher, but has features that improve both the Si and diamond etching: Rapid switching between chemistries allows for shorter steps in the so-called Bosch process, which alternates etching Si with SF_6 and passivating the walls with C_4F_8, leading to smoother etched walls in Si. In the diamond etching, a dense plasma and strong ion bombardment gives a high etch rate and more vertical walls. The etch rate is not particularly relevant for our application, but reducing the angle of the walls is important.

The Si etch process etched the hard-baked photoresist slowly, but fast enough that no separate etch step was required to remove the residual resist film from the SAMIM process. The process used an ICP RF power of 2000 W and 80 W chuck (bias) power with the chuck 120 mm below the ICP source. The two steps were 0.8 s with 300 sccm of C_4F_8 at 50 μbar and 2 s with 200 sccm SF_6 at 30 μbar. To account for some uncertainty in etch rate and residual layer thickness after SAMIM, the Bosch process was run several cycles longer than required to etch through the Si film with the diamond acting as an effective etch stop.

Diamond was etched in an oxygen plasma with both high ICP power and high bias power. The inductively coupled power was 2800 W, the chuck power was 300 W, and the chuck was positioned 150 mm below the plasma source. The high ICP power gave a dense plasma with many reactive ions and the high bias power pulled these ions towards the surface to impact the sample with high energy. In general, increasing the ICP power increases etch rate, and increasing chuck power and/or reducing the pressure increases etch rate and reduces the wall angle. At very high power and low pressure the mask can start to erode rapidly while at the opposite end, at lower power and higher pressure, the redeposition of mask material often causes micro-masking and a spiky texture on etched surfaces. The pressure for etching the AGPMs was 15 μbar, which gave a low enough etch rate in Si while producing side-walls with a small angle. To etch the AGPM to the correct depth, an etch test was first carried out to obtain a rough estimate of the etch rate in diamond. The AGPM substrate was then etched together with small diamond monitor samples. After stopping the etching deliberately short, a monitor sample was cracked and the cross section imaged by scanning electron microscope (SEM). The AGPM was then etched further based on the width, depth and wall angle observed in the monitor sample. After etching, remaining mask material was stripped in a HF/HNO_3 solution.

The anti-reflective grating on the back side of the component was patterned and etched in the same way as the AGPM. Since the depth of this grating is much smaller, we used a Si mask that was one third as thick. For the diamond etching the chuck power was reduced to 150 W and pressure was increased to 40 μBar. This increases the wall angle, but this is not a problem for a shallow grating and the slower etching gives better control over depth.

After final cleaning the AGPMs were tested at CEA Saclay, France. The test bench at the Astrophysics Division at CEA Saclay is a unique facility that has been primarily developed for the testing of the imager of the JWST/MIRI instrument. It allows measurements at cryogenic temperature from 5 μm to 30 μm wavelength. It has been adapted to fulfil the requirements for the testing of the METIS N-band phase masks [23]. In particular, we use quantum cascade lasers (QCLs), instead of a classical blackbody-like source. They provide a few mW of nearly monochromatic light, so one can achieve a high signal to noise ratio in a few seconds of integration time. This makes the process of centring the source on the mask more efficient.

The masks were measured at five wavelengths provided by five QCLs: 8.0, 9.0, 10.5, 11.5 and 12.5 μm. For each mask and each wavelength, a set of photometric references (i.e. point spread functions at some distance from the mask centre) were taken.[2] The source was then moved at the centre of the mask, and an automatic scan made hundreds of integrations on a fine raster pattern. From photometric analysis of the images, we found the position for which the null depth was the best.

The very stable environment inside the cryogenic facility, and the temperature controlled QCLs ensure a high repeatability of the measurements. However, uncertainties remain. They are primarily caused by the spatial variation of the photometric response, due to interferences inside the diamond plate of the mask itself. The long coherence length of the laser light makes these interferences possible. Consequently, it is difficult to know precisely the amount of energy in the photometric references, and one can only measure an average value with a rather high uncertainty. In the end, taking all sources of noise into account, the null depth was estimated with a typical error between 20 and 30 %, which is sufficient to estimate the grating parameters.

The grating parameters were estimated from the optical measurements by comparing null depth spectra calculated with RCWA to the measured values. By also considering that the grating parameters should be close to those measured by SEM, the most likely parameters can be found. The mean null depth spectrum changes slowly along diagonals in the depth-width plot that parallel the dashed line in Fig. 2 Left, which means that the uncertainty in parameters is greatest along these.[3] Luckily a change in the parameters along such a curve does not change how much the depth should be adjusted.

These tests determined that two of the three N-band AGPMs could be improved by reducing their depth. The following procedure was carried out on both of them. The AGPM was covered with photoresist (Shipley S1813) and then spun on a spin coater to remove excess resist (6000 rpm, 30 s). After baking for 10 min at 100 °C, the AGPM was again spin coated with photoresist and baked. This filled the grating while leaving the top with only a thin layer of photoresist. The component was then etched by oxygen plasma in a PlasmaTherm SLR system, in a chamber otherwise used for aluminium etching. This was a much gentler plasma than the one used to etch the grating originally: 900 W ICP power, 120 W chuck bias power with a 40 sccm O_2 flow and a pressure of 5 mTorr (6.7 μbar). After etching for 100 s, the photoresist in the grating was topped up by spin coating and baking again. The AGPM was then etched another 100 s. Remaining photoresist was removed by leaving the component in acetone for 48 h and (after rinsing) cleaning for 45 min in hot piranha solution. This process is similar to that used previously for reducing grating depth [6], but the chamber geometry and parameters for the plasma etching were changed. The chamber used here has the chuck 10 cm closer to the plasma and the bias power was lowered to 120 W instead of 200 W.

3. Results and discussion

Three N-band AGPMs were made. These are named VPM-MET-N, for Vortex Phase Mask – METIS – N-band, and the number etched at the edge of the front side of the substrates: #4, #8 and #9. In the rest of this paper we will refer to them as simply N4, N8 and N9. Due to poor quality of the first batch of diamond substrates delivered (of #1–5 only #4 was deemed good enough), several months passed between making the first component (N4) and the other two (N8 and N9). During the time in between the ICP etcher had problems with the matching network and cooling and went through a thorough service and changes in the software. This resulted in some differences between N4 and N8/N9 that are difficult to pinpoint the reason for.

Tests with a range of photoresist thicknesses in the SAMIM process found that a 1:1 ratio of resist in edge bead remover gave a thin residual resist film (few tens of nm) and no voids in the pattern (Fig. 4 Left). The resist thickness in the grating lines after baking was ~350 nm. Despite the cleaning procedure, there remained some small particles on the substrates. These both gave rise to thickness variations when spin coating and prevented the PDMS from contacting the surface during SAMIM. The defects caused by particles are therefore larger than the

[2] More details are available in the online supplementary material.

[3] An example is available in the supplementary material.

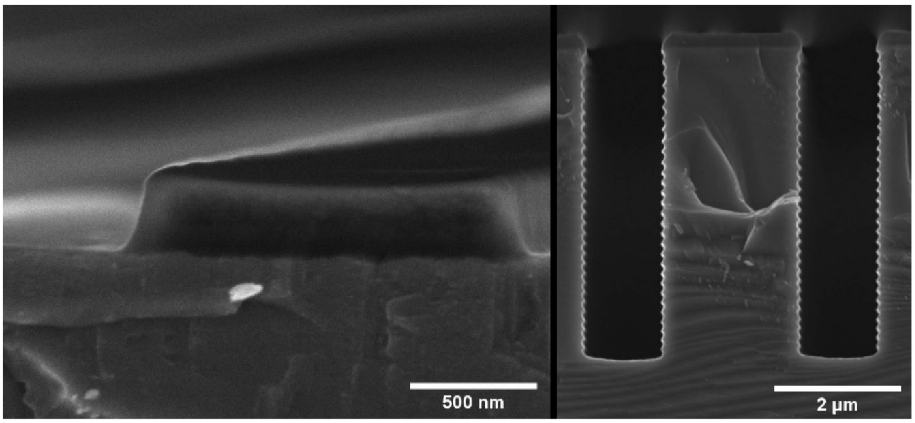

Fig. 4. Left: Cross section of photoresist on sputtered Si after SAMIM, showing the residual photoresist film on the left and a grating line on the right. Right: Cross section after 120 s (43 cycles) Si etch test. 30 steps are seen in the sidewall, so 13 cycles were needed to remove the residual resist before Si etching could start.

particles themselves. N9 had the most such defects, though smaller than the 50 µm maximum size specified for the inner part of the component.

Silicon test etching showed that the residual resist film was etched through after 10–15 cycles, after which Si was etched at a rate of 160–180 nm/cycle (slowed down a bit when etching deeper, Fig. 4 Right). A 90 s (32 cycles) etch time was chosen for the AGPM mask, which was enough to etch through the 2.2 µm thick Si film with a few cycles margin to compensate for uncertainties in the residual film thickness and Si etch rate.

After diamond etching and cleaning, the AGPMs had very little variation in line width across the component. Compared to previous N-band components, the edges were smoother which we attribute to the smoother Si mask compared to Al. In previous N-band AGPMs small line width deviations could also be found along some angles, which we took to be due to astigmatism during the laser lithography. No such deviations could be seen here, an effect of switching to electron beam lithography. Fig. 5 shows the center of the N4 AGPM and one of the AGPMs made for NEAR [19] for comparison.

The main difference between etching N4 compared to N8 and N9 was the etch rate in diamond. When etching N8 and N9, the etch rate was 430 nm/min compared to 360 nm/min when etching N4 (these etch rates are averages, the rate slows with depth). The Si removal rate, however, decreased during diamond etching. As can be seen in the cross-section micrographs in Fig. 6 a and b, Si is primarily removed through sputtering at the edges of the mask, giving rise to a faceted top. With almost the same etched depth in diamond, the amount of Si removed during the N8/N9 etching was only half that of the N4 etching. This material is partially re-deposited on the opposite wall of the trench (Fig. 6a), narrowing the opening which in turn increases the wall angle (1.3° on the N4 monitor piece). When etching N8 and N9 there was barely any re-deposited material (Fig. 5b), leading to nearly vertical walls (0.7°). As noted above, we are not sure what caused this difference in the etching, possibly it was due to differences in cooling caused by a malfunctioning helium flow controller when etching N8/N9. All three components had much steeper walls than previous N-band AGPMs and we had no problem reaching the depth and aspect ratio required. For comparison, a monitor sample from etching the AGPMs for NEAR [19], where we used an Al mask, is shown in Fig. 6c. The Al mask was sputtered in a much more focused manner than Si onto the opposing wall, leading to a higher wall angle (3.2°). Besides the wall angle, the whole etched AGPM gratings can be a bit slanted, as can be seen in Fig. 6. Such an angle should have minimal effect on the performance according to RCWA calculations.

The grating depth estimated from the monitor pieces after diamond etching was 13.4 µm for N4 and 13.1 µm for N8 and N9, with an estimated error margin of around 300 nm. The optical testing of the components showed that N8 and N9 were likely ~800 nm too deep. This can be either because the depth was under-estimated, or because the line width or effective wall angle was over-estimated. This in turn can be both due to small mis-measurements in the SEM micrographs of the monitor cross section and due to differences between the monitor and the AGPM. The grating cross section is not a perfect trapezoid as in the simulations, so lines were fitted by eye to estimate the effective width and angle. In particular the effective wall angle can be difficult to estimate and an error as small as 0.1° can change the optimal depth by hundreds of nanometers.

The anti-reflective gratings on the back side of the components had a depth of 1.65–1.7 µm and the width of the asperities was 2.2–2.3 µm, with a wall angle of around 2°. This should reduce the mean back side reflection below 1.5 % and the maximum reflection at the edge of the wavelength band below 4 %.[4]

The changes implemented in the process to reduce grating depth (reducing bias power and having the plasma closer to the chuck) gave flatter, less faceted tops in the grating and also improved the etch rate ratio between diamond and resist (Fig. 7). Since the upper part of the sidewall gets exposed to the plasma during the process, the width can also be slightly reduced. As can be seen in Fig. 7, the photoresist remaining in the grooves can be a bit uneven and contain small voids. We have not seen that this affects the grating as long as the etch steps between refilling the grooves are kept short.

We repeated the optical measurements on the N8 and N9 AGPMs after reducing the grating depth, in the very same manner as the first measurements. Both masks behaved very similarly to each other. As expected, the performance at 8.0, 9.0, 10.5 and 11.5 µm was greatly improved while it was reduced at 12.5 µm (Fig. 8). Estimating the grating parameters based on the optical measurements, the effective line width seems to have been reduced. It is also possible that the depth reduction was smaller than in the etch test, which would give a very similar spectrum, as explained in the methods section. The overall performance was the best measured for an N-band vortex phase mask to date.

4. Conclusion

Three high performing broad band AGPMs for the N-band (8.1–13.1 µm) have been produced. The realisation of these required etching higher aspect ratio gratings than previous such components, which in turn required etching with more vertical walls. This was made possible by changing the mask material from Al to Si, which does not cause as much redeposited material to build up on the sides of the etched

[4] More details of the anti-reflective grating are available in the online supplementary material.

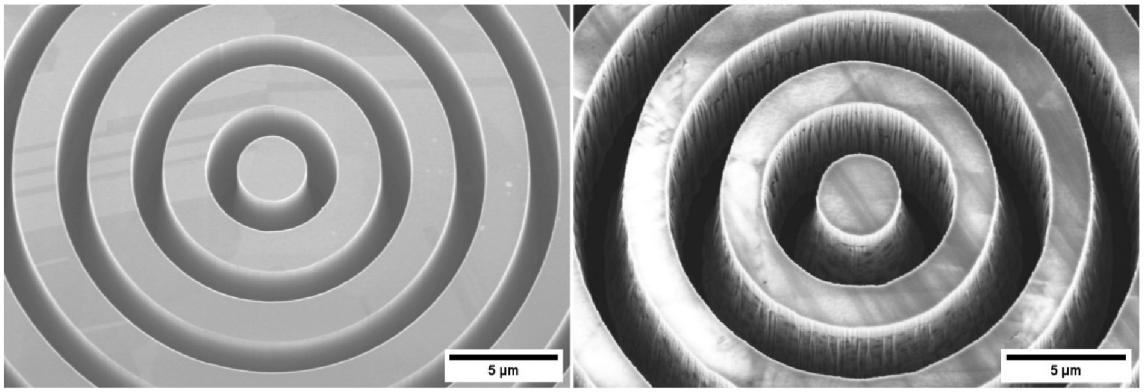

Fig. 5. View of the center of the AGPM. Left: the new N4 component. Right: one of the AGPMs manufactured for NEAR [19] using laser lithography for the master pattern and Al for the mask.

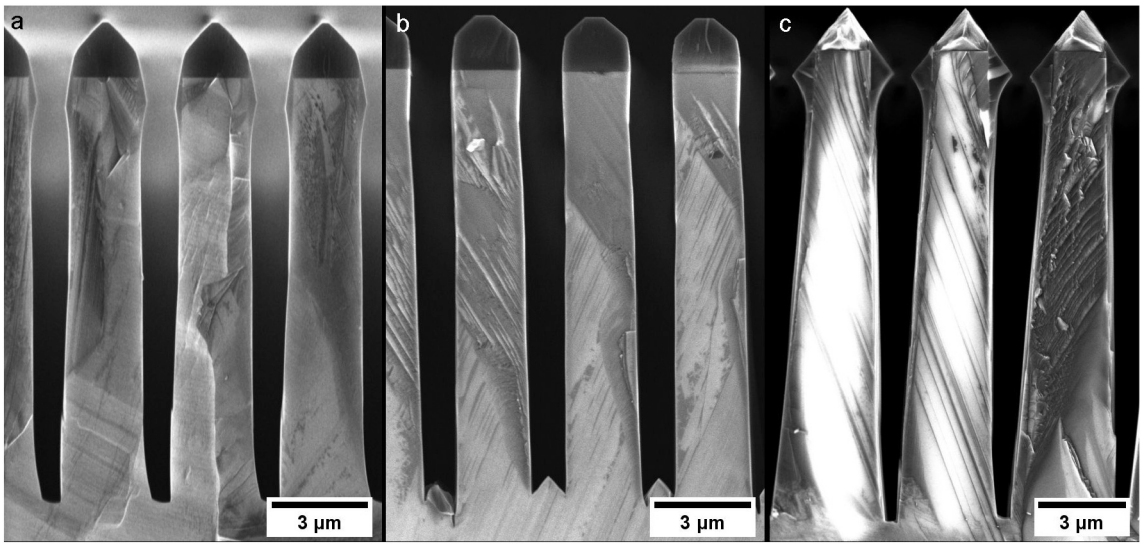

Fig. 6. Cross section SEM micrographs of monitor pieces from etching AGPM gratings. (a) From etching N4. (b) From etching N8 and N9. (c) From etching one of the NEAR [19] AGPMs with an Al mask, included for comparison. Note that the period of the grating in (c) is 4 µm while it is 3.4 µm in (a) and (b).

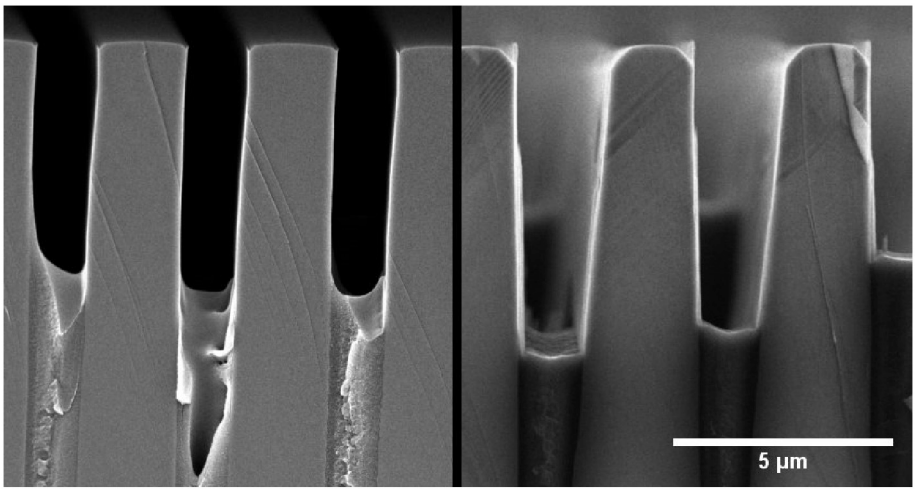

Fig. 7. Comparison of cross section after depth reduction, showing the top of the grating and grooves partially filled with photoresist. Left: Etch test for reducing the depth of N8 and N9 (depth reduced by ~800 nm). Right: Etch test for reducing the depth of one of the NEAR [19] AGPMs (depth reduced by ~1 µm). The new depth reduction process used on the left clearly gives much less faceting at the top of the grating.

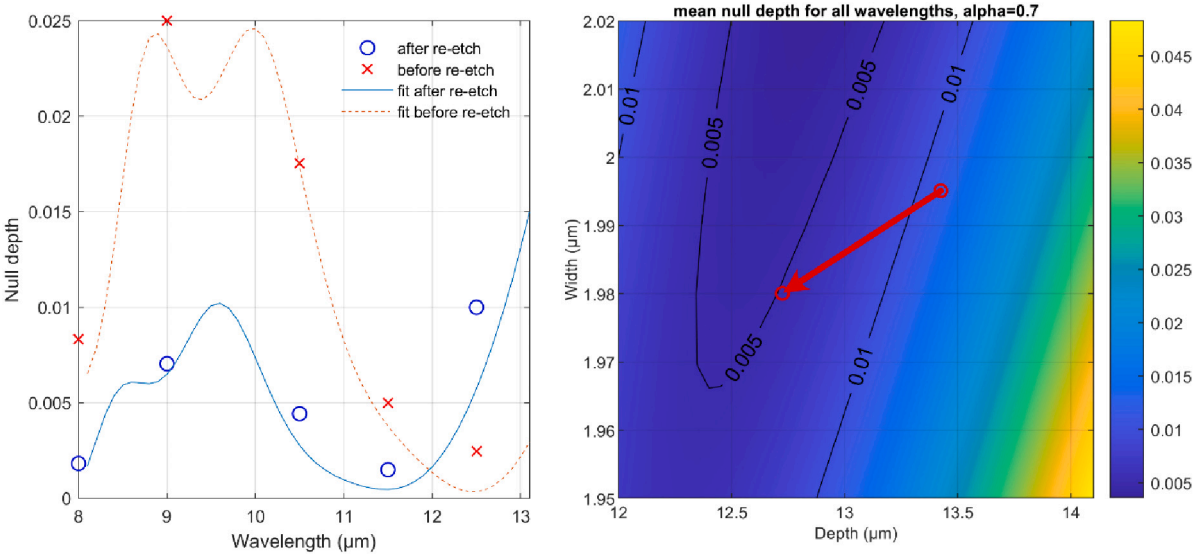

Fig. 8. Left: Measured and calculated performance of the N8 AGPM. The red crosses were measured before reducing the grating depth and the blue circles after. The lines are calculated using RCWA with our best estimates of grating parameters based on both the optical and SEM measurements: blue solid line a = 0.7°, h = 12.725 μm, w = 1.98 μm; red dashed line a = 0.7°, h = 13.425 μm, w = 1.995 μm. Right: Null depth map for a wall angle of 0.7°. The parameter estimates have been marked by circles and the arrow shows the result of the depth reduction. (For interpretation of the references to colour in this figure legend, the reader is referred to the web version of this article.)

grooves, and increasing the bias power during etching. Optical testing in the new cryogenic test bench with QCL laser sources allowed us to estimate the grating parameters with sufficient precision that the components could be greatly improved by adjusting the depth. This means that the METIS instrument at the ELT will be equipped with the best N-band vortex phase masks to date.

4.1. Future

At the time of writing, these components are awaiting installation in the METIS instrument.

Diamond has an absorption band from 2- and 3-phonon interactions around 5 μm. While it is not a very strong absorption, the overlap with the M-band makes diamond less than ideal for this wavelength band. In the future we will investigate using other materials or very thin diamond substrates for this band. Reducing the thickness of the diamond substrate will make the component more fragile and difficult to work with, but it will let us use the same etch process. In the extreme case, a thin diamond film may be used or even an unsupported grating [24] though this would require connecting the rings of the AGPM grating. Using a different material will require a new fabrication process. As mentioned under AGPM design above, IR transparent materials with suitable refractive index may be difficult to etch and require a lot of process development.

We have seen some indication that the etch rate varies slightly (up to around 1 %) between crystal grains in the diamond. We used a mix of physical and chemical etching with reactive ions impacting the surface at high speed. When chemical etching dominates (i.e. the bias power is low), diamond can be etched crystallographically [11,12], so a small difference in etch rate is not surprising even when the etching has a strong physical component. To reach even higher precision, future AGPMs may benefit from being etched in single crystal diamond [5]. This may also help reduce both bulk and surface defects, since many of them stem from grain boundaries.

Author statement

The authors have all approved the contents of the paper and confirm that this original manuscript is not previously published or under consideration for publication elsewhere.

CRediT authorship contribution statement

Pontus Forsberg: Writing – review & editing, Writing – original draft, Visualization, Supervision, Software, Methodology, Investigation, Conceptualization. **Petri Karvinen:** Writing – review & editing, Resources, Methodology, Investigation. **Samuel Ronayette:** Writing – review & editing, Software, Methodology, Investigation. **Markku Kuittinen:** Writing – review & editing, Resources, Methodology, Funding acquisition. **Olivier Absil:** Writing – review & editing, Supervision, Project administration, Funding acquisition, Conceptualization. **Lorenzo König:** Investigation. **Christian Delacroix:** Investigation. **Gilles Orban de Xivry:** Project administration. **Jean-Christophe Barriere:** Project administration. **Eric Pantin:** Supervision, Resources, Project administration. **Mikael Karlsson:** Writing – review & editing, Supervision, Resources, Project administration, Methodology, Investigation, Funding acquisition, Conceptualization.

Declaration of competing interest

The authors declare that they have no known competing financial interests or personal relationships that could have appeared to influence the work reported in this paper.

Data availability

Data will be made available on request.

Acknowledgements

The authors gratefully acknowledge funding from the Research Council of Finland Flagship Programme, Photonics Research and Innovation (PREIN), decision number 346518 and the Swedish-French Foundation. This project has received funding from the European Research Council (ERC) under the European Union's Horizon 2020 research and innovation programme (grant agreement No 819155), and the European Southern Observatory.

Appendix A. Supplementary data

Supplementary data to this article can be found online at https://doi.org/10.1016/j.diamond.2024.111237.

References

[1] ESO, "Top Level Requirements for ELT-MIDIR", Document Number ESO-204695 Version 2. https://www.eso.org/sci/facilities/eelt/docs/ESO-204695_2_Top_Level_Requirements_for_ELT-MIDIR.pdf, 2015.

[2] D. Mawet, P. Riaud, O. Absil, J. Surdej, Annular Groove Phase Mask 633, ApJ, 2005, p. 1191, https://doi.org/10.1086/462409.

[3] D. Mawet, L. Pueyo, D. Moody, J. Krist, E. Serabyn, The Vector Vortex Coronagraph: sensitivity to central obscuration, low-order aberrations, chromaticism, and polarization, in: SPIE Astronomical Telescopes + Instrumentation, 2010, p. 773914, https://doi.org/10.1117/12.858240.

[4] A.M. Zaitsev, Optical Properties of Diamond: A Data Handbook, Springer, 2001, https://doi.org/10.1007/978-3-662-04548-0.

[5] P. Forsberg, M. Karlsson, High aspect ratio optical gratings in diamond, Diam. Relat. Mater. 34 (2013) 19–24, https://doi.org/10.1016/j.diamond.2013.01.009.

[6] E. Vargas Catalán, E. Huby, P. Forsberg, A. Jolivet, P. Baudoz, B. Carlomagno, C. Delacroix, S. Habraken, D. Mawet, J. Surdej, O. Absil, M. Karlsson, Optimizing the subwavelength grating of L-band annular groove phase masks for high coronagraphic performance, in: A&A 595 A127, 2016, https://doi.org/10.1051/0004-6361/201628739.

[7] E. Vargas Catalán, P. Forsberg, O. Absil, M. Karlsson, Controlling the profile of high aspect ratio gratings in diamond, Diam. Relat. Mater. 63 (2016) 60–68, https://doi.org/10.1016/j.diamond.2015.08.007.

[8] E. Vargas Catalán, P. Piron, A. Jolivet, P. Forsberg, C. Delacroix, E. Huby, O. Absil, I. Vartiainen, M. Kuittinen, M. Karlsson, Subwavelength diamond gratings for vortex coronagraphy: towards an annular groove phase mask for shorter wavelengths and topological charge 4 designs, Opt. Mater. Expr. 8 (7) (2018) 1976–1987, https://doi.org/10.1364/OME.8.001976.

[9] G.S. Sandhu, W.K. Chu, Reactive ion etching of diamond, Appl. Phys. Lett. 55 (1989) 437–438, https://doi.org/10.1063/1.101890.

[10] M. Karlsson, F. Nikolajeff, Diamond micro-optics: microlenses and antireflection structured surfaces for the infrared spectral region, Opt. Express 11 (5) (2003) 502–507, https://doi.org/10.1364/OE.11.000502.

[11] M. Mitchell, D.P. Lake, P.E. Barclay, Realizing Q > 300 000 in diamond microdisks for optomechanics via etch optimization, APL Photon. 4 (2019) 016101, https://doi.org/10.1063/1.5053122.

[12] M. Kiss, T. Graziosi, A. Toros, T. Scharf, C. Santschi, O.J.F. Martin, N. Quack, High-quality single crystal diamond diffraction gratings fabricated by crystallographic etching, Opt. Express 27 (21) (2019) 30371–30379, https://doi.org/10.1364/OE.27.030371.

[13] A. Toros, M. Kiss, T. Graziosi, S. Mi, R. Berrazouane, M. Naamoun, J. Vukajlovic Plestina, P. Gallo, N. Quack, Reactive ion etching of single crystal diamond by inductively coupled plasma: state of the art and catalog of recipes, in: Diamond & Related Materials 108, 2020, p. 107839, https://doi.org/10.1016/j.diamond.2020.107839.

[14] D.T. Tran, C. Fransler, T.A. Grotjohn, D.K. Reinhard, J. Asmussen, Investigation of mask selectivities and diamond etching using microwave plasma-assisted etching, Diam. Relat. Mater. 19 (2010) 778–782, https://doi.org/10.1016/j.diamond.2010.02.001.

[15] P. Kehayias, A. Jarmola, N. Mosavian, I. Fescenko, F.M. Benito, A. Laraoui, J. Smits, L. Bougas, D. Budker, A. Neumann, S.R.J. Brueck, V.M. Acosta, Solution nuclear magnetic resonance spectroscopy on a nanostructured diamond chip, Nat. Commun. 8 (2017) 188, https://doi.org/10.1038/s41467-017-00266-4.

[16] M. Makita, P. Karvinen, V.A. Guzenko, N. Kujala, P. Vagovic, C. David, Fabrication of diamond diffraction gratings for experiments with intense hard X-rays, Microelectron. Eng. 176 (2017) 75–78, https://doi.org/10.1016/j.mee.2017.02.002.

[17] K. Li, Y. Liu, M. Seaberg, M. Chollet, T.M. Weiss, A. Sakdinawat, Wavefront preserving and high efficiency grating beam splitter for X-ray free electron laser, Opt. Express 28 (2020) 10939–10950, https://doi.org/10.1364/OE.380534.

[18] E. Serabyn, E. Huby, K. Matthews, D. Mawet, O. Absil, B. Femenia, P. Wizinowich, M. Karlsson, M. Bottom, R. Campbell, B. Carlomagno, D. Defrère, C. Delacroix, P. Forsberg, C. Gomez Gonzalez, S. Habraken, A. Jolivet, K. Liewer, S. Lilley, P. Piron, M. Reggiani, J. Surdej, H. Tran, E. Vargas Catalán, O. Wertz, The W. M. Keck Observatory Infrared Vortex Coronagraph and a First Image of HIP 79124 B 153, AJ, 2017, p. 43, https://doi.org/10.3847/1538-3881/153/1/43.

[19] K. Wagner, A. Boehle, P. Pathak, M. Kasper, R. Arsenault, G. Jakob, U. Käufl, S. Leveratto, A.-L. Maire, E. Pantin, R. Siebenmorgen, G. Zins, O. Absil, N. Ageorges, D. Apai, A. Carlotti, É. Choquet, C. Delacroix, K. Dohlen, P. Duhoux, P. Forsberg, E. Fuenteseca, S. Gutruf, O. Guyon, E. Huby, D. Kampf, M. Karlsson, P. Kervella, J.-P. Kirchbauer, P. Klupar, J. Kolb, D. Mawet, M. N'Diaye, G. Orban de Xivry, S.P. Quanz, A. Reutlinger, G. Ruane, M. Riquelme, C. Soenke, M. Sterzik, A. Vigan, T. de Zeeuw, Imaging low-mass planets within the habitable zone of α Centauri, Nat. Commun. 12 (2021) 922, https://doi.org/10.1038/s41467-021-21176-6.

[20] M. Moharam, D. Pommet, E. Grann, T. Gaylord, Stable implementation of the rigorous coupled-wave analysis for surface-relief gratings: enhanced transmittance matrix approach, J. Opt. Soc. Am. A 12 (1995) 1077–1086, https://doi.org/10.1364/JOSAA.12.001077.

[21] C. Delacroix, O. Absil, P. Forsberg, D. Mawet, V. Christiaens, M. Karlsson, A. Boccaletti, P. Baudoz, M. Kuittinen, I. Vartiainen, J. Surdej, S. Habraken, Laboratory demonstration of a mid-infrared AGPM vector vortex coronagraph, in: A&A 553 A98, 2013, https://doi.org/10.1051/0004-6361/201321126.

[22] L. König, O. Absil, M. Lobet, C. Delacroix, M. Karlsson, G. Orban de Xivry, J. Loicq, Optimal design of the annular groove phase mask central region, Opt. Express 30 (15) (2022) 27048–27063, https://doi.org/10.1364/OE.461047.

[23] S. Ronayette, S. Mouzali, J.-C. Barrière, É. Pantin, T. Orduna, P. Gallais, M. Lortholary, L. Dumaye, O. Absil, C. Delacroix, D. Ives, M. Karlsson, An N-band test bench for the METIS coronagraphic masks, in: SPIE Astronomical Telescopes + Instrumentation 114472U, 2020, https://doi.org/10.1117/12.2562261.

[24] P. Forsberg, M. Malmström, E.V. Catalan, M. Karlsson, Diamond grating waveplates, Opt. Mater. Expr. 6 (6) (2016) 2024–2030, https://doi.org/10.1364/OME.6.002024.